








Asteroseismology of luminous red giants with *Kepler* I: Long Period Variables with radial and non-radial modes

Jie Yu ^{1,2,3*}, Timothy R. Bedding ^{1,3}, Dennis Stello ^{4,1,3}, Daniel Huber ^{5,1,3}, Douglas L. Compton ^{1,3}, Laurent Gizon ^{2,6,7}, and Saskia Hekker ^{2,3}

¹*Sydney Institute for Astronomy (SIFA), School of Physics, University of Sydney, NSW 2006, Australia*

²*Max Planck Institute for Solar System Research, Justus-von-Liebig-Weg 3, 37077 Göttingen, Germany*

³*Stellar Astrophysics Centre, Department of Physics and Astronomy, Aarhus University, Ny Munkegade 120, DK-8000 Aarhus C, Denmark*

⁴*School of Physics, University of New South Wales, NSW 2052, Australia*

⁵*Institute for Astronomy, University of Hawai'i, 2680 Wood-lawn Drive, Honolulu, HI 96822, USA*

⁶*Institut für Astrophysik, Georg-August-Universität Göttingen, Friedrich-Hund-Platz 1, 37077 Göttingen, Germany*

⁷*Center for Space Science, NYUAD Institute, New York University Abu Dhabi, PO Box 129188, Abu Dhabi, UAE*

Accepted XXX. Received YYY; in original form ZZZ

ABSTRACT

While long period variables (LPVs) have been extensively investigated, especially with MACHO and OGLE data for the Magellanic Clouds, there still exist open questions in their pulsations regarding the excitation mechanisms, radial order and angular degree assignment. Here, we perform asteroseismic analyses on LPVs observed by the 4-year *Kepler* mission. Using a cross-correlation method, we detect unambiguous pulsation ridges associated with radial fundamental modes ($n = 1$) and overtones ($n \geq 2$), where the radial order assignment is made by using theoretical frequencies and observed frequencies. Our results confirm that the amplitude variability seen in semiregulars is consistent with oscillations being solar-like. We identify that the dipole modes, $l = 1$, are dominant in the radial orders of $3 \leq n \leq 6$, and that quadrupole modes, $l = 2$, are dominant in the first overtone $n = 2$. A test of seismic scaling relations using Gaia DR2 parallaxes reveals the possibility that the relations break down when $\nu_{\max} \lesssim 3 \mu\text{Hz}$ ($R \gtrsim 40 R_{\odot}$, or $\log L/L_{\odot} \gtrsim 2.6$). Our homogeneous measurements of pulsation amplitude and period for 3213 LPVs will be very valuable for probing effects of pulsation on mass loss, in particular in those stars with periods around 60 days, which has been argued as a threshold of substantial pulsation-triggered mass loss.

Key words: stars: oscillations, stars: evolution, stars: late-type, techniques: photometric

1 INTRODUCTION

Long Period Variables (LPVs)¹ are cool evolved stars on the asymptotic giant branch or near the tip of the red giant branch. They are generally divided into Semiregular Variables (SRs) and Mira variables, based on the regularity and amplitudes of their light curves. Major advances in the understanding of pulsations in LPVs have been achieved from studying their period–luminosity (P–L) diagrams, using ground-based surveys such as MACHO (Wood et al.

1999), EROS (Lebzelter et al. 2002), and OGLE (Soszyński et al. 2004; Soszyński et al. 2009), and space missions like *Hipparcos* (Bedding & Zijlstra 1998; Tabur et al. 2010), CoRoT (Lebzelter 2011; Ferreira Lopes et al. 2015), *Kepler* (Bányai et al. 2013; Mosser et al. 2013; Hartig et al. 2014; Stello et al. 2014), and Gaia (Mowlavi et al. 2018; Lebzelter et al. 2018). While the pulsation sequences of LPVs have been extensively studied, the nature of the pulsations is still not fully understood.

The first open question is linked to the driving mechanism of the pulsations in SRs: self-excitation via a heat-engine mechanism like Mira variables, or stochastically excited as solar-like oscillations in G and K stars? One method to investigate excitation mechanisms of LPVs is to analyze the relation between the pulsation amplitude and period, and compare with less-luminous red giants that are well-

* E-mail: yujie@mps.mpg.de (JY)

¹ In this work, we use these three terms interchangeably: LPVs, M giants, and high-luminosity red giants, though the first is extended to include pulsators with periods down to a few days, and the second is extended to include some late K giants.

established to be sun-like oscillators (e.g. Tabur et al. 2010). Soszynski et al. (2007) proposed that stars falling along their so-called sequences b2 and b3 are sun-like pulsators (see the sequences in Figure 4a). Mosser et al. (2013) argued that all the P–L relations for LPVs can be explained by solar-like oscillations, in that the P–L sequences are an extension of a global oscillation pattern in less-evolved red giants. This is consistent with the findings by Dziembowski & Soszyński (2010) and Takayama et al. (2013) and but discrepant to the predictions by Xiong et al. (2018). However, Bányai et al. (2013) argued that Mira/Semiregular variables may have a pulsation nature different from sun-like oscillations. This is based on their findings of a significant pulsation-amplitude transition at a period of ~ 10 days, a dividing point between SRs and shorter-period solar-like pulsators. We note that Ferreira Lopes et al. (2015, their Figure 3) found a similar amplitude-transition feature, which, however, may be attributed to the different amplitude definitions between their work and the comparison reference. In this work, we find evidence in support of solar-like oscillations in SRs (see Section ??).

The second question concerns assigning radial orders to the pulsation sequences on the P–L diagram. Soszynski et al. (2007), Dziembowski & Soszyński (2010), and Mosser et al. (2013) interpreted the sequences C', B, and A as the radial fundamental mode, first overtone, and second overtone, respectively (see the sequences in Figure 4a). This means the longer-period sequence C, containing Mira variables, has no interpretation in terms of radial orders if we assume that two adjacent sequences differ by one radial order. However, a distinct set of radial order assignment from Wood et al. (1999), Soszyński & Wood (2013), Takayama et al. (2013), and Wood (2015) state that sequences C, C', and B are associated with the radial fundamental mode, first overtone, and second overtone, respectively. Thus, the two sets of modal assignments differ by one radial order. Recently, Trabucchi et al. (2017) re-examined the observed P–L sequences and gave an intermediate solution that C' and B both correspond to the first overtone, but include fundamental mode pulsations at lower luminosities of the two sequences. They suggested that sequences C, A, and A' correspond to the radial fundamental mode, second overtone, and third overtone, respectively. We discuss this issue in Section 6.

The third question concerns the angular degree of the modes. Do LPVs exhibit radial and non-radial pulsations? And which modes are dominant, radial modes ($l = 0$), dipole modes ($l = 1$), or quadrupole modes ($l = 2$)? Soszynski et al. (2004) discovered that the sequence A consists of three closely separated parallel subsequences in the so-called Petersen diagram, where the ratio of a shorter period to a longer period is plotted against the longer period. The subsequences were later also found in the sequence B and A' by Soszynski et al. (2007). Stello et al. (2014) found a triplet frequency pattern in *Kepler* M giants that is made up of $l = 1, 2, 0$ modes, sorted in the decreasing period order. This triplet pattern explains the parallel subsequences in the Petersen diagram. Mosser et al. (2013) further argued that dipole modes dominate in stars oscillating at higher frequency ($\gtrsim 1.0 \mu\text{Hz}$), while radial modes dominate at lower frequency ($\lesssim 1.0 \mu\text{Hz}$). However, Stello et al. (2014) found that the pulsations of luminous *Kepler* stars with a characteristic oscillation frequency down to $0.2 \mu\text{Hz}$ are dominated

by dipole modes. The findings from Wood (2015, Figure 3) using the OGLE III catalog of LPVs in the LMC is in agreement with the findings by Stello et al. (2014). We address this issue in Section 7.

The fourth question is related to the asteroseismic scaling relations. The relations have been widely used to characterize oscillating dwarfs and giants (see Chaplin et al. 2013; Hekker & Christensen-Dalsgaard 2017, for reviews). Moreover, asteroseismically derived parallaxes have been used as references to calibrate the Gaia DR2 parallaxes (e.g. Zinn et al. 2019). Although the seismic scaling relations have been extensively tested on main-sequence stars, subgiants, and less-luminous red giants (for a recent review, see Hekker 2019), it remains an open question if the relations work for high-luminosity red giants (see Section 8).

In this work we address these four open questions using a sample of 3213 *Kepler* LPVs, which includes pulsators with periods $P \gtrsim 1$ day. Our asteroseismic analyses are based on the light curves collected by the 4-year *Kepler* space mission (Borucki et al. 2010; Koch et al. 2010) and on Gaia DR2 parallaxes (Lindgren et al. 2018).

2 SAMPLE SELECTION AND DATA REDUCTION

To construct a sample of LPVs, we selected 4296 *Kepler* red giants from Mathur et al. (2017) with surface gravity $\log g < 2.0$ dex, equivalent to a period $\gtrsim 1$ day. We added known *Kepler* M giants from the literature, namely, Bányai et al. (2013), Stello et al. (2014), and Yu et al. (2018). For the sample in Yu et al. (2018), we applied a cut of $\nu_{\text{max}} \leq 15 \mu\text{Hz}$. Note that the M giants collected from the literature also meet the criterion of periods $\gtrsim 1$ day.

From the sample of 4724 stars selected above, we excluded the stars with marginal pulsation detections. This is because 75% of them have too short light curves for our analyses, i.e., they were observed for fewer than 4 quarters, and/or too faint, the *Kepler* magnitudes $K_p > 14$ mag. For the other 25% of the excluded stars (that is, 8% stars in the original sample), no clear pulsation signal is found. It has been known that for some stars, which can be bright and have long time series, solar-like oscillations are expected but not detected (e.g. see Chaplin et al. 2011; Mathur et al. 2019; Schonhut-Stasik et al. 2019). We note that Schonhut-Stasik et al. (2019) reported the same fraction for red giants (8%) without solar-like oscillation detections. Our final sample comprised 3213 LPVs, as listed in Table 1.

Kepler long-cadence photometry is well-suited for exploring pulsations in LPVs, given its temporal sampling rate (29.4 min) and long baseline (~ 4 years). We used PDCSAP light curves, which have been corrected for systematic errors in each observing quarter using ‘cotrending basis vectors’ (Stumpe et al. 2012; Smith et al. 2012). For some M giants pulsating at a long period, such as Mira variables, PDCSAP time series were over-corrected, by treating intrinsic pulsations as ‘systematic errors’. For these stars, we adopted ‘Simple Aperture Photometry’ (SAP) light curves. To determine the stars for which the PDCSAP light curves were safe to use, we used a measure, P_{extrema} , which approx-

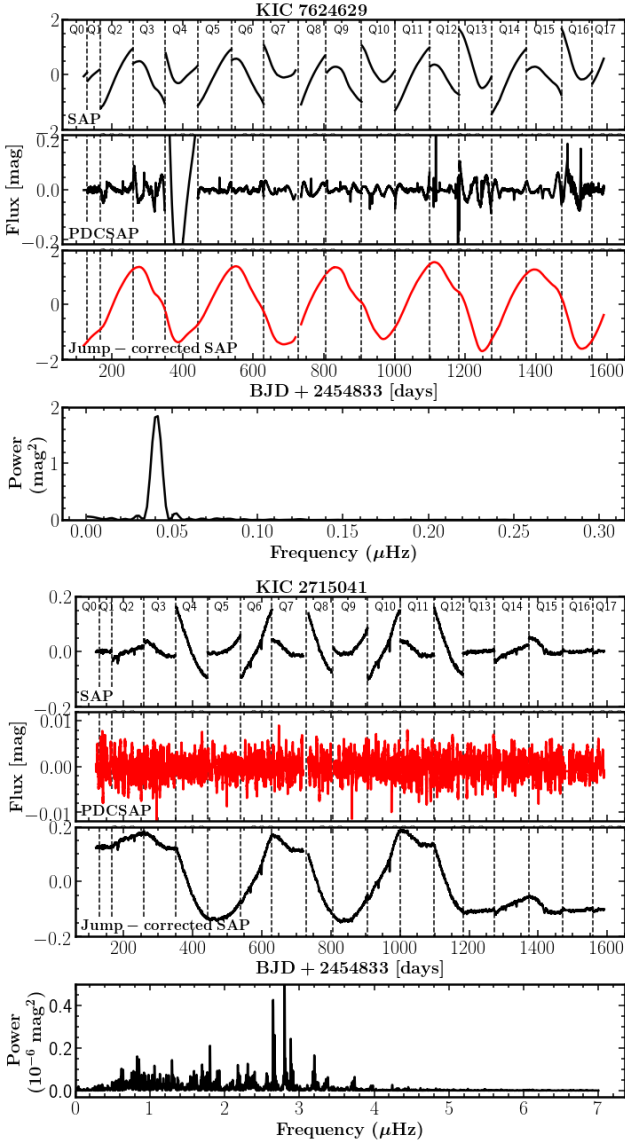


Figure 1. Light curves for two representative *Kepler* LPVs: KIC 7624629 (upper, slow pulsator) and KIC 2715041 (lower, fast pulsator). For each star, the SAP (1st panel), PDCSAP (2nd panel), and jump-corrected SAP (3rd panel) light curves are shown. The light curves in red were adopted for asteroseismic analyses. The bottom panel of each star shows the power spectrum, computed from the adopted light curves. In this work, all power spectra were calculated in units of square micro-magnitude. Our spectrum normalisation ensures that we measured the amplitude of a sinusoidal wave.

imates a typical period of a light curve. It is defined as

$$P_{\text{extrema}} = \frac{2N\delta t}{N_{\text{extrema}}}, \quad (1)$$

where N_{extrema} is the number of turning points (extrema), N is the total number of data points of a light curve, and δt is the sampling interval of the long-cadence *Kepler* data (29.4 min).

To count the turning points in a light curve, we calculated the point-to-point difference of the light curve. The

number of the zero crossings of the difference time series gives the number of turning points. Since there are quarter gaps in *Kepler* light curves, which will introduce turning points between quarter edges because the corresponding flux usually jumps dramatically, we then performed iterative $4\text{-}\sigma$ clipping to discard outliers of the difference time series. Finally, we found $P_{\text{extrema}} = 6$ days is an appropriate threshold to select the light curve source (PDCSAP versus SAP). We have tested different thresholds of P_{extrema} up to 30 days, and found the conclusions below were not changed significantly. This is because our method for preparing light curves also works well in the short-period range where PDCSAP light curves were used.

For PDCSAP time series with $P_{\text{extrema}} < 6$ days, we divided each quarter of time series by its median flux, and concatenated them together. For SAP data, we used a Gaussian Process method (Rasmussen & Williams 2006) to remove jumps between two adjacent quarters for stars with $P_{\text{extrema}} > 6$ days. A step function was used to model jumps and a covariance function was used to approximate the residuals, due to actual physical brightness variations as well as noise. We implemented the Gaussian process fit using *CELERITE* and the kernel *SHOTerm* (Foreman-Mackey et al. 2017). Note that systematic perturbations, such as spacecraft safe-mode events and/or long-term drifts, could affect light curves but were not corrected considering their much lower amplitudes than the intrinsic stellar variability. Stars for which we detected periods equal to one *Kepler* orbit (372 d) were discarded. We hereafter refer to a star as a slow pulsator if $P_{\text{extrema}} > 6$ days or as a fast pulsator if $P_{\text{extrema}} \leq 6$ days.

Figure 1 shows the jump-corrected SAP light curve (red curve) and its power spectrum, for a representative slowly pulsating M giant, KIC 7624629 (top 4 panels), with $P_{\text{extrema}} = 198.41$ days. The PDCSAP time series for this star was clearly over-corrected. Figure 1 also shows the SAP and PDCSAP light curves for a typical fast pulsating star, KIC 2715041 (bottom 4 panels), with $P_{\text{extrema}} = 3.36$ days. For this star, we can see that systematic annual perturbations in the PDCSAP light curve have been nicely removed. The jump-corrected SAP light curve for this star is clearly dominated by annual instrumental drifts.

For the fast and slow samples, we used different methods to measure the pulsation period and amplitude of the dominant modes. For pulsators in the slow sample, we first measured the period of the highest peak in the power spectrum of the difference time series. Note that a difference time series is essentially free from the quarter jumps in the associated light curve, since the jumps manifest themselves as outliers that can be clipped. In order to measure the amplitude, we then searched the power spectrum of the time series for the highest peak in a window with a width of 10 times the frequency resolution and centered at the frequency measured from the difference time series. The height of the highest peak was used as a proxy for the amplitude.

For stars in the fast sample, we first used the SYD pipeline (Huber et al. 2009) to measure the frequency of maximum oscillation power, ν_{max} . We subsequently selected the highest peak within a window centered at ν_{max} . The width of this window was the full-width-at-half-maximum of a Gaussian fitted to the auto-correlation of the oscillation power excess. These steps are necessary, because for a fast oscillator the dominant mode generally is not the highest

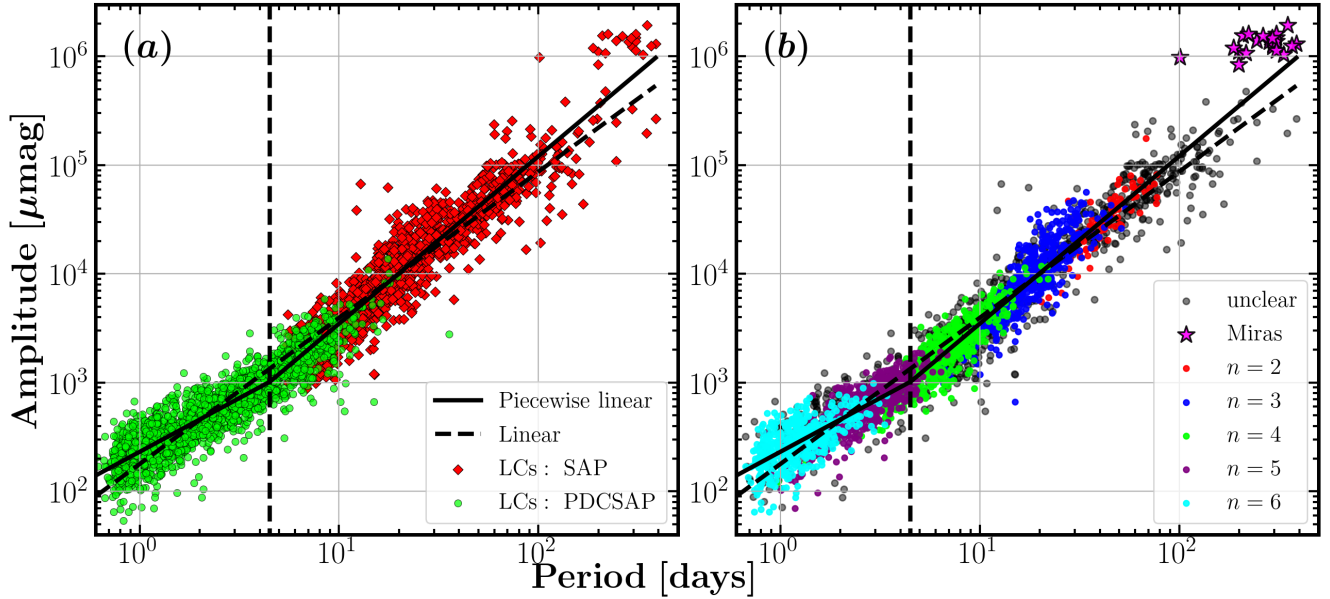


Figure 2. (a) Relation between the period and amplitude proxy of the dominant mode, i.e., the highest peak in a power spectrum. Periods and amplitudes were extracted from either PDCSAP time series shown in green circles, or jump-corrected SAP time series indicated in red diamonds (see the text). The piecewise linear model (solid), preferred to the linear model (dashed), shows a kink at period $P \approx 4.5$ days, indicated in the vertical dashed line. (b) Similar to (a) now color-coded by the radial order of the dominant mode.

peak in the power spectrum, due to $1/f$ noise in the lower frequency regime. This is unlike a slow pulsator, such as a Mira variable, for which the highest peak generally is the dominant mode. Again, we used the height of the highest peak as a proxy to approximate the amplitude. We note that the amplitude of a dominant mode contains the contributions from the granulation background, which is the case for both fast and slow pulsators.

To understand the impact of the background, we calculated the ratio of the height of the dominant mode to the amplitude of granulation at the frequency of the dominant mode. The granulation amplitude was calculated from the fitted background obtained when measuring the global seismic parameters, ν_{\max} and $\Delta\nu$, using the SYD pipeline (see Section 6.1). We found that this ratio is approximately constant, consistent with Mosser et al. (2013, see their Figure 4), and has a median value of 5.9. This suggests that our measured proxy of the oscillation amplitudes globally overestimates the amplitude by $\sim 20\%$ ²

3 PERIOD–AMPLITUDE RELATION OF LONG PERIOD VARIABLES

Figure 2a shows our measured amplitude proxy versus periods for the entire sample. At the longest periods we see a number of Mira variables with periods $P > 100$ days and amplitude near 1.0 mag (also shown in the pink asterisks in Figure 2b). We also see SRs, with periods typically longer

than 20 days and lower amplitudes. Note that in this work we measured the amplitude of a sinusoidal wave, which is half of the peak-to-peak amplitude. Miras are characterized by pulsation periods longer than 100 days and peak-to-peak amplitudes greater than 2.5 mag at visual wavelengths. Here, for Mira variables a typical measured peak-to-peak amplitude is 2.0 mag, smaller than the 2.5 mag definition, which is because of the redder and broader *Kepler* bandpass (e.g. see Lund 2019, and references therein). Both period and amplitude, together with additional parameters, are listed in Table 1.

Figure 2b illustrates the period-amplitude relation color-coded by the radial order of the dominant mode, which was determined as discussed in Section 6.1. We provide radial order assignment only down to $n = 2$ using model frequencies from Stello et al. (2014). We can see that at the boundaries the adjacent radial orders overlap. This is caused by the stochastic excitation nature of the oscillation modes. For some stars their dominant modes can be non-radial modes and can be a few radial orders away from ν_{\max} , which leads to n spanning a larger period range.

We fitted a piecewise linear model and a linear model to the measured relation between the period and amplitude proxy of the dominant mode, and found the former model is preferred due to its smaller Akaike information criterion (AIC) and Bayesian information criterion (BIC). Figure 2 reveals a break point at period $P = 4.5$ days, determined by the piecewise linear model fit. Pulsation amplitude increases more rapidly for $P > 4.5$ days.

Figure 3 shows the dominant mode amplitude as a function of period and as a function of P_{extrema} for $P_{\text{extrema}} > 6$ days, respectively. We can see that the parameter P_{extrema} has a tight relation with the amplitude, and is a very good proxy of the dominant mode period (note the similarity of

² Since $(O+B)/B=5.9$, i.e., $O/B=4.9$, one obtains $H/O=(O+B)/O=1.2$. Here, H, O, B denote the height of the highest peak, the oscillation amplitude proxy, and the granulation amplitude at the highest peak, respectively.

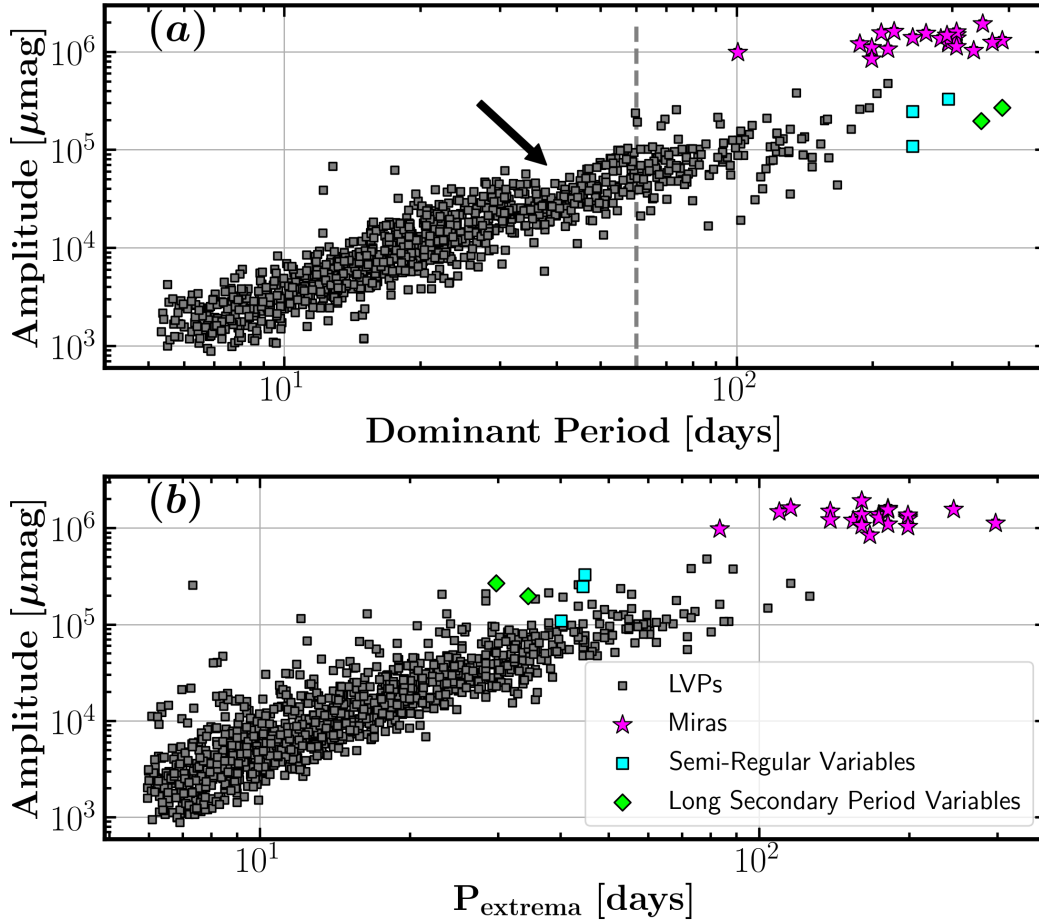


Figure 3. (a): Relation between amplitude and period for stars with periods greater than 6 days, thus dominated by SRs and Mira variables. The dashed line marks the approximate period threshold, 60 days, above which substantial pulsation-triggered mass loss is expected. (b): Relation between amplitude and P_{extrema} for the same stars. All the Long secondary period variables and Miras in the entire sample are highlighted, while only two representative SRs are shown.

the horizontal axes). All the Miras, two Long Secondary Period (LSP) variables, and three representative SRs are highlighted. We can see that the SRs and LSPs are significantly shifted toward the left in the lower panel while the Miras are much less shifted. This is because SRs and LSPs show more variations in addition to their main periodicity, and thus have more turning points. Figure 3a shows a significant amplitude decrease at $P \approx 40$ days (the black arrow), which coincides with the radial-order transition of dominant modes from $n = 3$ to $n = 2$, i.e. from pulsation sequence A to B (see Figures 2b and 4b). Figure 3b reveals a sharper lower boundary along the global trend than Figure 3a. This feature is mainly due to dilution of the oscillation power excess caused by contamination of nearby or foreground/background stars, leading to lower amplitude and smaller P_{extrema} .

Note that P_{extrema} can be computed from light curves and are hardly affected by *Kepler* quarter jumps (by sigma clipping). It could be a robust measure for searching for SRs and Miras observed by the *TESS* mission (Ricker et al. 2015), in particular those LPVs in the continuous viewing zones. We emphasize that this large and homogeneous sample of LPVs is excellent to study mass-loss triggered by pulsation

directly (Yu et al. in preparation). A period of 60 days has been argued as a threshold above which substantial dust mass loss is expected (see McDonald et al. 2018, and references therein). This investigation will be carried out in the second paper of this series.

4 PERIOD–LUMINOSITY RELATION

Over the past two decades, one of the major advances in the investigation of LPVs has been the detection of pulsation sequences on the P–L diagram using MACHO and OGLE data. Here, we combine the *Kepler* and OGLE LPVs as shown in Figure 4. Figure 4a shows a Period– M_K diagram of the LPVs in the LMC, where only the dominant period from the OGLE-III catalogue is used (Soszyński et al. 2009). The absolute 2MASS K magnitude, M_K , was computed from the Gaia DR2 parallaxes using the same method as Huber et al. (2017) and Berger et al. (2018). We adopted a LMC distance modulus of 18.54 mag and an extinction $A_V = 0.38$ mag (Imara & Blitz 2007). Sequences A', A, B, C', and C are labeled, following the nomenclature of Soszynski et al. (2007). Figure 4b shows that the vast majority of the *Kepler*

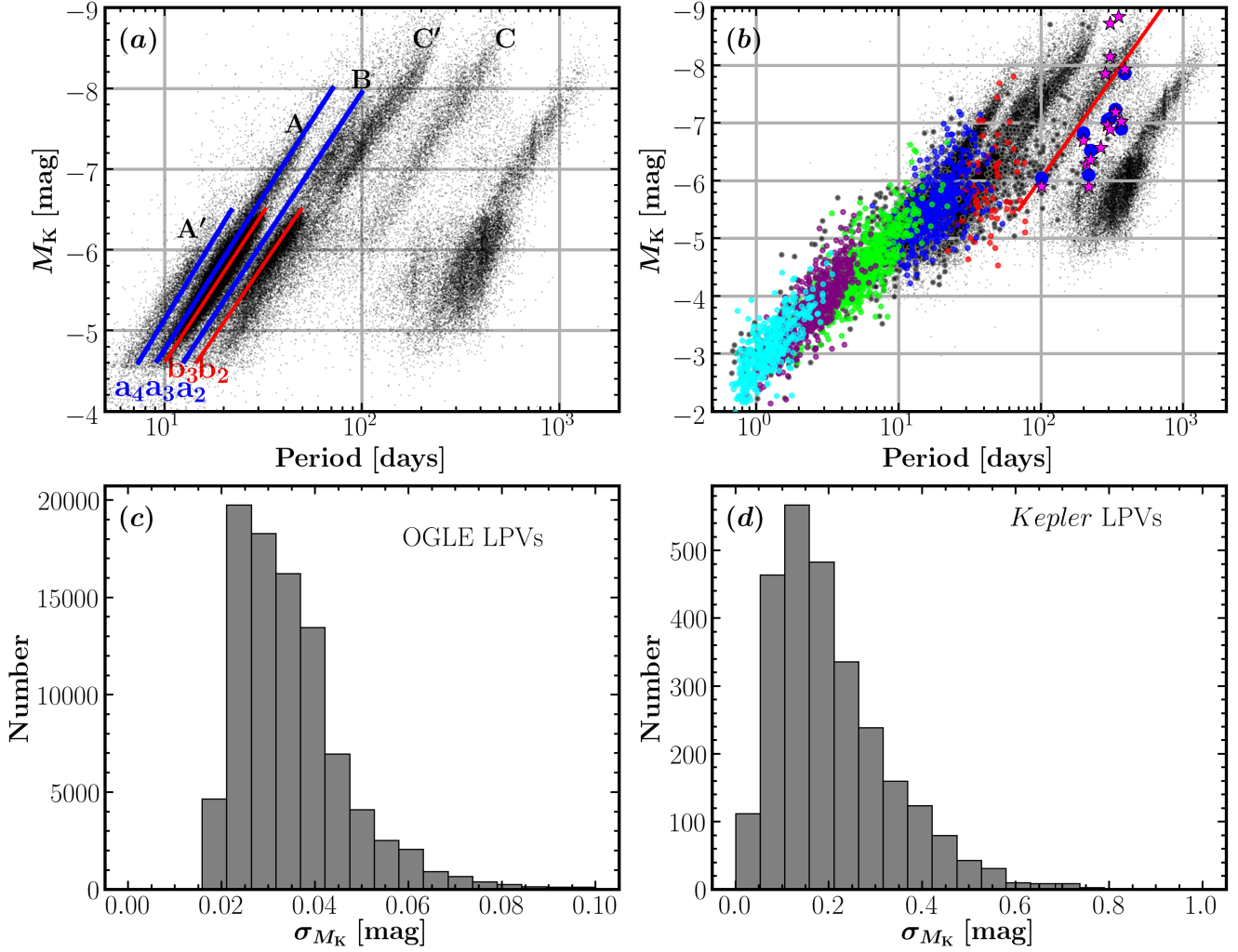


Figure 4. (a) Period- M_K diagram of OGLE LPVs (black points) in the LMC (dominant mode only, Soszyński et al. 2009). For OGLE small amplitude red giants, sequences a_2 , a_3 , and a_4 denoting AGB stars are shown in blue lines, while sequences b_2 and b_3 denoting red-giant-branch (RGB) stars are shown in red lines (the line parameters were adopted from Table 1 of Soszynski et al. 2007). (b) Similar to panel a now including the *Kepler* LPVs (Note the difference in the scale of the vertical and horizontal axes). Symbol colors have the same meaning as Figure 2b. Miras with Gaia DR2 parallaxes better than 30% are highlighted in the dark blue circles. The red line denotes the Period- M_K relation for Miras (Feast 1996). (c) Uncertainties of M_K for the OGLE LPVs. (d) Uncertainties of M_K for the *Kepler* LPVs.

$n = 3, 4$ LPVs (green and blue) occupy the same region in the P-L diagram as the sequences A, A'. However, the *Kepler* results do not show the well-defined sequences of OGLE LPVs. This is more likely due to the approximately six times larger M_K uncertainties, as revealed by Figures 4c and 4d. We do nevertheless expect the pulsation sequences in *Kepler* LPVs to be the underlying pattern in Figure 4, given that we have detected radial and non-radial sequences over several radial orders (plotted in a difference way, see Section 6).

We calculated the distances in the Period- M_K diagram of all $n = 3$ LPVs (most are RGB stars) to sequences b_2 and b_3 , and found they are globally closer to sequence b_3 rather than b_2 . This tells us that sequence A of the OGLE stars possibly corresponds to the second overtone, while the sequences B and C' could be the first overtone. (Note that sequence A comprises sequences a_3 for AGB stars and b_3 for

RGB stars.) *Kepler* Miras are near sequence C. Our findings are consistent with the theoretical results by Trabucchi et al. (2017), and provide an intermediate solution of radial order assignment over the two sets of contradictory suggestions (see the second open question reviewed in Section 1).

5 STOCHASTIC VS MIRA-LIKE EXCITATION IN SEMIREGULAR VARIABLES

To address the question of mode excitation in SRs, we consider the properties characterizing solar-like oscillations. If a detected mode is resolved into a Lorentzian profile, its amplitude in the Fourier spectrum as normalised here (see the caption of Figure 1) decreases with increasing length of the time series. However, if a detected mode is unresolved,

Table 1. Asteroseismic parameters and stellar properties of *Kepler* M giants

KIC	LCs	Q	P_{extrema}	T_{eff} K	amp μmag	period day	order	ν_{max} μHz	$\Delta\nu$ μHz	π mas	d kpc	L L_{\odot}	A_v mag
(1)	(2)	(3)	(4)	(5)	(6)	(7)	(8)	(9)	(10)	(11)	(12)	(13)	(14)
892738	PDCSAP	18	nan	4534±135	308.24	1.44	6	7.47±0.25	1.31±0.01	0.40±0.02	2.490±0.137	193.96± 21.69	0.29
893210	PDCSAP	17	nan	4204±127	1004.15	4.36	5	2.62±0.05	0.51±0.01	0.23±0.03	4.440±0.503	574.52±133.14	0.25
893233	PDCSAP	8	nan	4207±147	903.45	1.94	5	6.16±0.08	1.18±0.01	0.43±0.03	2.338±0.151	227.36± 29.88	0.28
1026309	PDCSAP	18	nan	4514±80	97.86	0.77	6	16.09±0.91	1.92±0.01	0.67±0.02	1.502±0.048	178.02± 12.19	0.28
1026895	PDCSAP	18	nan	3900±80	714.65	3.88	5	2.78±0.11	0.54±0.01	0.83±0.02	1.214±0.036	445.50± 27.16	0.24
1027110	PDCSAP	18	nan	4190±80	466.93	1.62	6	6.67±0.14	1.15±0.01	0.33±0.02	3.019±0.194	187.73± 24.44	0.24
1027707	PDCSAP	18	nan	4254±148	872.85	3.87	4	3.03±0.04	0.54±0.01	0.17±0.03	5.739±0.841	654.15±198.06	0.23
1160655	PDCSAP	18	nan	3740±130	1715.10	7.28	4	1.63±0.02	0.37±0.01	0.38±0.03	2.631±0.181	253.08± 36.65	0.61
1160867	PDCSAP	18	nan	4000±80	550.43	2.56	4	4.68±0.08	0.89±0.01	1.12±0.03	0.893±0.022	240.36± 12.64	0.70
1160986	PDCSAP	4	nan	4347±80	193.40	0.99	7	8.85±0.62	1.54±0.02	0.21±0.02	4.688±0.334	134.51± 19.42	0.71
12600259	PDCSAP	18	nan	4288±150	283.99	1.38	6	7.69±0.2	1.36±0.02	0.35±0.02	2.872±0.204	162.86± 23.63	0.15
12600652	PDCSAP	18	nan	4056±141	1210.53	3.98	4	2.86±0.04	0.57±0.02	0.27±0.02	3.801±0.351	348.10± 65.53	0.13
12601040	SAP	18	32.30	3275±114	56380.99	67.45	2	nan	nan	0.26±0.06	3.996±0.918	1548.26±759.13	0.11
12602404	PDCSAP	10	nan	4457± 80	315.54	0.88	6	12.97±0.13	1.95±0.01	0.30±0.02	3.352±0.241	129.36± 18.96	0.27
12602421	SAP	18	7.80	4175±124	2346.49	7.94	nan	nan	nan	0.66±0.02	1.525±0.052	473.81± 33.76	0.27
12644223	PDCSAP	18	nan	4086±143	893.23	2.63	5	4.18±0.13	0.84±0.02	0.16±0.01	6.217±0.456	281.87± 41.99	0.20
12645224	SAP	18	12.66	4035±141	5338.09	11.78	nan	nan	nan	0.40±0.03	2.512±0.168	857.84±116.16	0.16
12688798	PDCSAP	6	nan	4245± 80	395.85	0.92	6	13.05±0.21	1.97±0.01	0.31±0.01	3.262±0.150	86.88± 8.27	0.15
12690711	SAP	18	6.38	3986±139	1422.41	7.26	nan	nan	nan	0.23±0.03	4.454±0.495	657.43±149.19	0.21
12984227	SAP	18	17.36	3489±122	9606.24	20.37	nan	nan	nan	0.28±0.04	3.670±0.534	880.49±264.38	0.20

Note. (1) KIC ID; (2) The type of light curve used in this work; (3) Number of quarters of *Kepler* light curves; (4) P_{extrema} (see Section 2 for its definition); (5) Source: Mathur et al. (2017); (6) Dominant mode amplitude; (7) Dominant mode period; (8) Radial order; (9) The frequency of maximum power; (10) Mean larger frequency separation; (11) Gaia DR2 parallax with an offset of 0.03 mas added (Lindegren et al. 2018); (12) (13) (14) Distance, Luminosity, and Extinction, respectively.

(This table is available in its entirety in machine-readable form.)

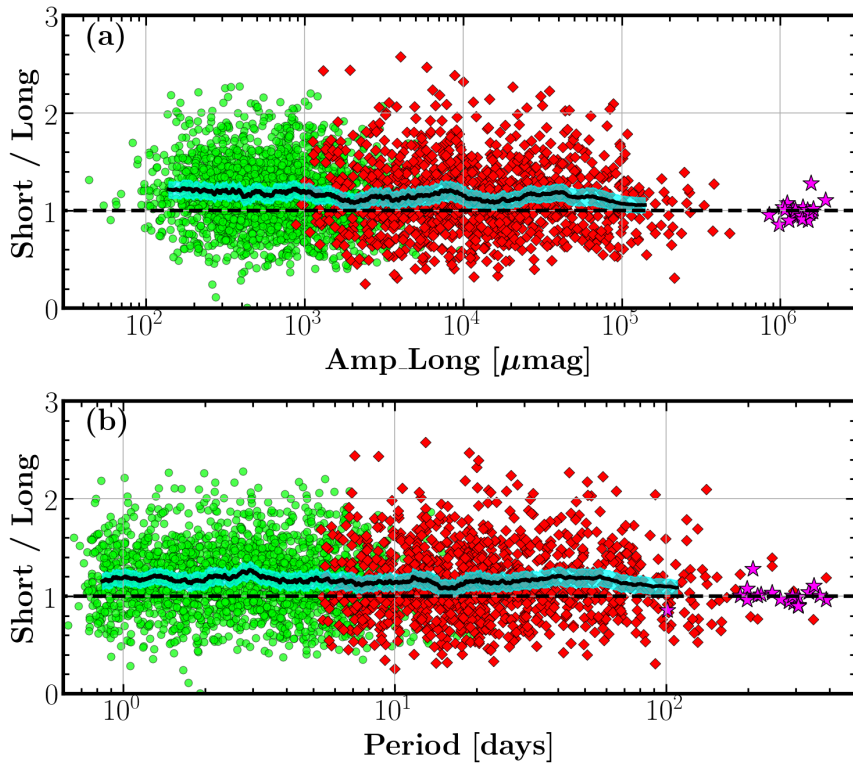


Figure 5. Comparison of the dominant mode amplitudes measured from full-length and a 1/3-length of the *Kepler* light curves. The top panel displays the amplitude ratio as a function of the amplitude measured from full-length light curves, while the bottom panel shows the ratio against period, also determined from full-length light curves. The running median values are shown in black and their 3- σ uncertainties are shown in the cyan filled region. Green and red symbols have the same meaning as Figure 2a. Miras are highlighted with the pink asterisks.

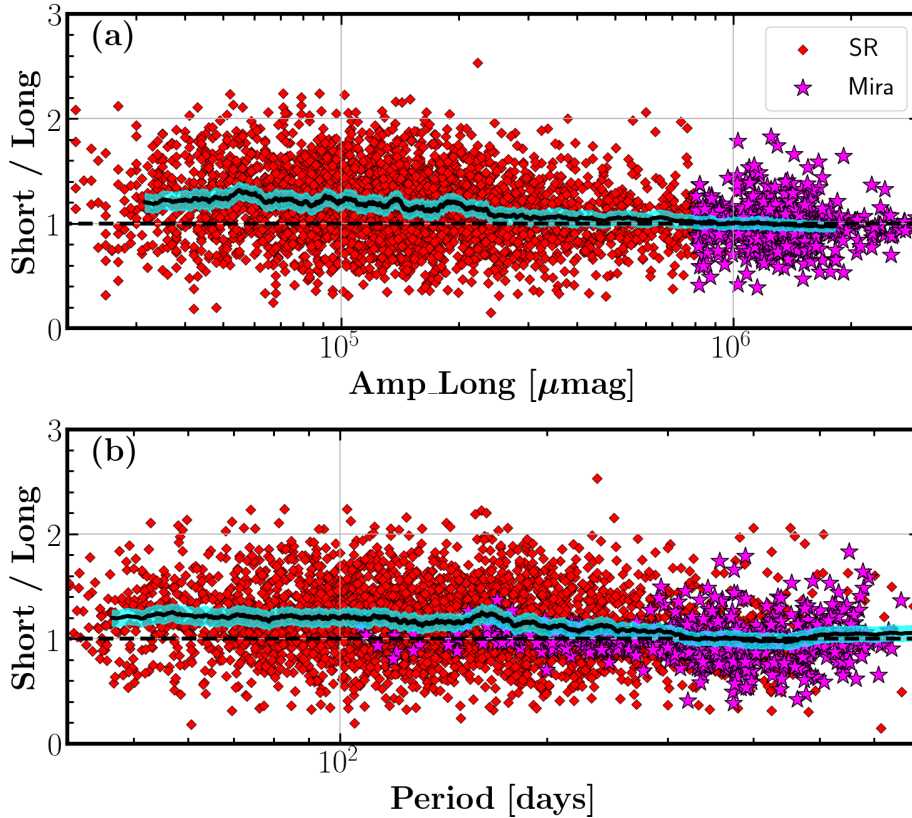


Figure 6. Similar as Figure 5 now using the *I*-band light curves of 3383 SRs (red diamonds) and 499 Miras (pink asterisks) in the OGLE-III catalog (Soszyński et al. 2009). These stars are selected to have light curve coverage longer than 10 years and a duty cycle greater than 0.4.

and hence can be described by a sinc function, its amplitude does not depend on the length of the time series. Bearing this in mind, we cut the total light curve for each star into three segments with equal length, and selected the one with the highest duty cycle to measure the pulsation period and amplitude in the same way as before (see Section 3).

Figure 5 shows a comparison of the dominant mode amplitudes, measured from the full-length and 1/3-length light curves. We observe clearly a systematic offset in the amplitude ratios when the amplitude is less than 0.1 mag, or $P \approx 70$ days, and good consistency in amplitude for the Miras. The scatter in the amplitude ratios is significantly larger for the SRs than for the Miras. The offset confirm that the pulsations are stochastically excited in SRs and self-excited in Miras (Christensen-Dalsgaard et al. 2001; Bedding 2003).

The expected amplitude ratio is $\sqrt{3}$ if the modes are completely resolved, and unity if the modes are unresolved. Our measured ratio for the SRs is ~ 1.2 , which is smaller than the expected value, indicating the modes are partially resolved. The ratio decreases slowly with increasing amplitude, showing that the intrinsic mode lifetimes increases slowly.

To test whether the systematic offset of the amplitude ratio is statistically significant, we performed a two-sided one sample t-test against the stars with the amplitude smaller than 0.1 mag. Our null hypothesis was that there is no significant difference between the “short” and “long” amplitudes, namely the amplitude ratio is unity. We found

that the t-statistic value is 26.7, the degrees of freedom is 3139, and the p-value is 2.1×10^{-141} . The p-value is far less than the significance level $\alpha = 0.05$, so we rejected the null hypothesis. This means that the “short” amplitudes are significantly larger than the “long” amplitudes in a statistical sense.

We note that for the *Kepler* Miras and longest period SRs, the *Kepler* light curves cover only a few cycles. Thus, we investigated the amplitude ratio of SRs and Miras in the OGLE III catalog that have light curve coverage longer than 10 years and a duty cycle greater than 0.4. Using the same method as for the *Kepler* LPVs, we found very similar offsets of the amplitude ratio, as shown in Figure 6, and therefore further supports the conclusion that we see a transition from predominantly stochastic-excitation in SRs to a more coherent self-excitation mechanism in Miras as we found from the *Kepler* LPVs.

6 RADIAL ORDER ASSIGNMENT

6.1 Radial order assignment by theoretical frequencies

Figures 7 and 8 show the stacked power spectra of 2000 stars with clearly detected oscillations, for which the ν_{\max} values are in the range $0.14 \mu\text{Hz} \leq \nu_{\max} \leq 10.54 \mu\text{Hz}$ (period 1.1–82 d). For this, we used dedicated procedures (see below)

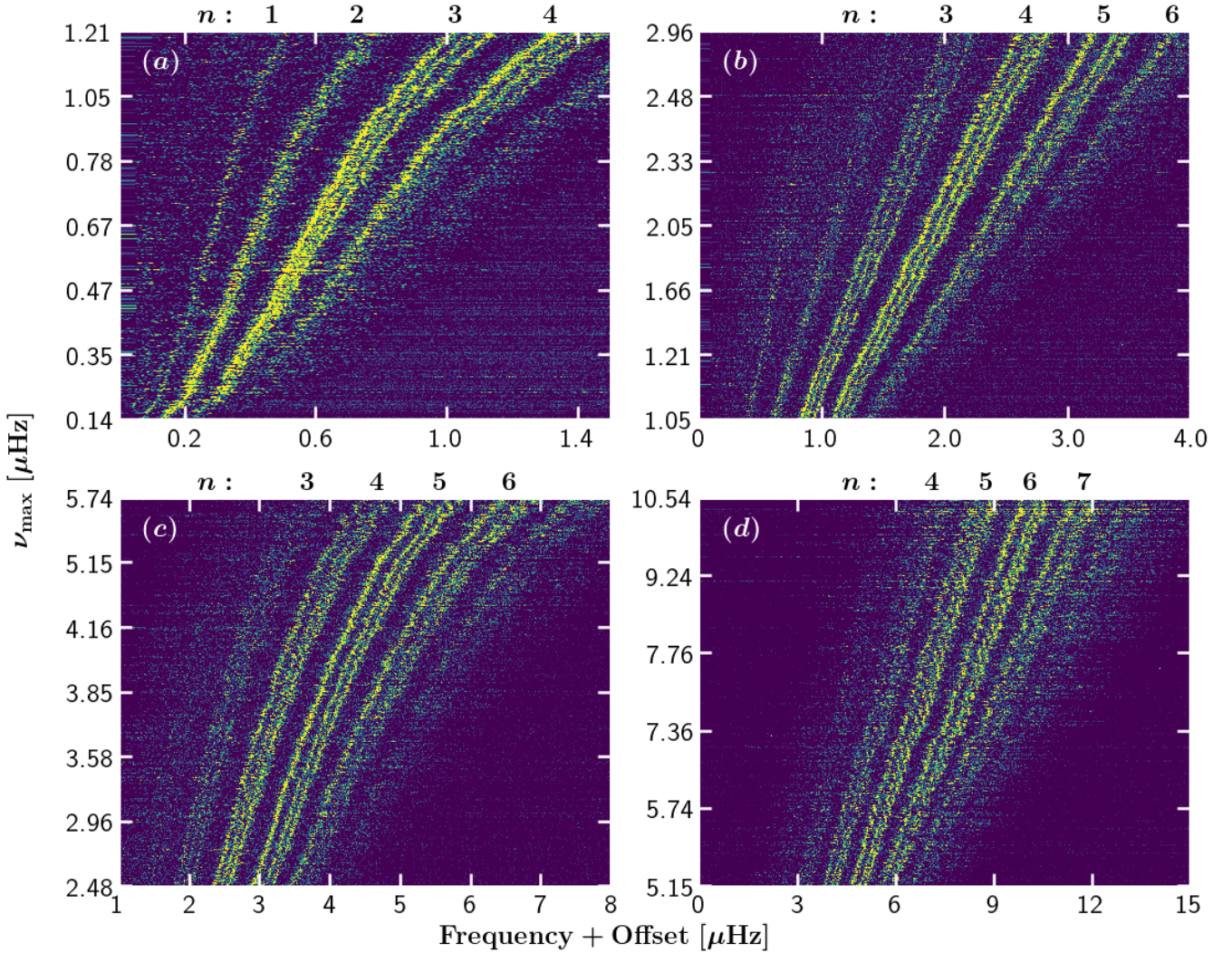


Figure 7. Stacked power spectra of high-luminosity red giants with $0.14 \mu\text{Hz} \leq \nu_{\text{max}} \leq 10.54 \mu\text{Hz}$. The stacked spectra are shown in four panels so as to highlight in different ν_{max} ranges clear ridges associated with multiple angular degrees over several radial orders. Each horizontal band represents one power spectrum with the power color-coded. The ordinate axis is not linear in ν_{max} , hence the different ridge curvatures in the different panels. For each radial order $n \geq 3$, as indicated at the top of each panel, $l = 1, 2, 0$ modes lie along the left, middle, and right ridge, respectively.

to detect the clear pulsation ridges corresponding to multiple angular degrees $l = 0, 1, 2$ for a number of radial orders $1 \leq n \leq 7$. The basic idea in constructing these ridges is to construct a series of template power spectra as references, and then shift an observed target power spectrum to align with the references. The method is summarized as follows.

(i) We used the SYD pipeline (Huber et al. 2009) to prepare background-divided power spectra, and to measure global seismic parameters, ν_{max} and $\Delta\nu$.

(ii) We then created template spectra using the model frequencies from Stello et al. (2014). They calculated the stellar models for a fixed stellar mass of $1M_{\odot}$ ³ at solar metallicity, using the MESA `1M_pre_ms_to_wd` test suite

case (Paxton et al. 2011, 2013)⁴. Their adiabatic frequencies were calculated using ADIPLS (Christensen-Dalsgaard 2008). Both ν_{max} and $\Delta\nu$ were derived from seismic scaling relations for each stellar model. From the frequencies of a given stellar model, we built a template spectrum, where each mode was described by a Lorentzian profile and its height was modulated by a Gaussian envelope. The Gaussian envelope was centered at ν_{max} with a standard deviation of $\Delta\nu$, hence $\text{FWHM} \approx 2.4 \Delta\nu$. Both ν_{max} and $\Delta\nu$ were subsequently interpolated with 100-times finer step sizes, as well as the associated model frequencies. The model frequencies from Stello et al. (2014) were only available for models with $\nu_{\text{max}} \geq 0.2 \mu\text{Hz}$. We linearly extrapolated the model frequencies for ν_{max} down to $0.1 \mu\text{Hz}$. This extrapolation only

³ This approaches a median mass of $1.2 M_{\odot}$ for our sample.

⁴ A detailed description of the implemented physics is given by Stello et al. (2014) and references therein.

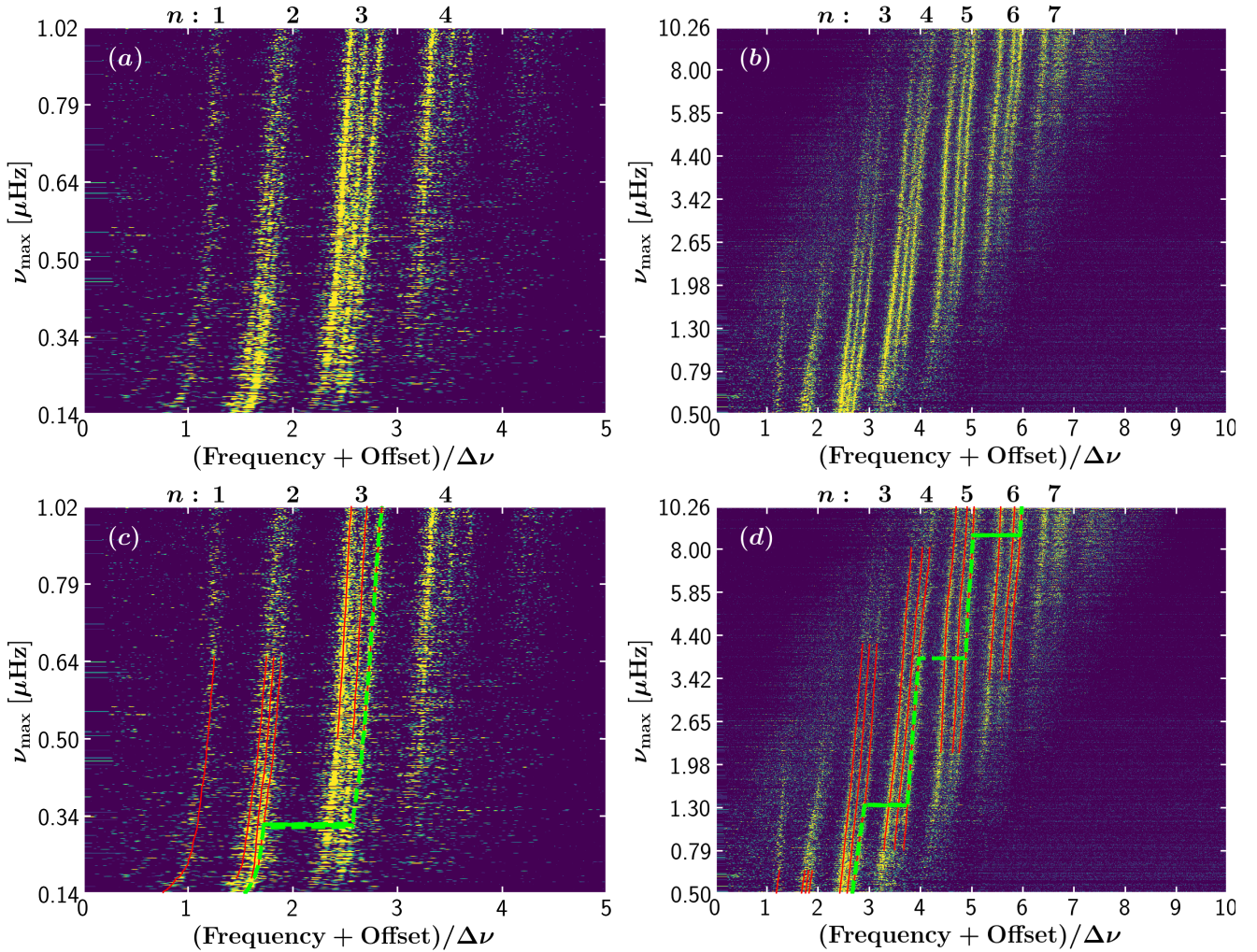


Figure 8. Similar to Figure 7, except that the horizontal axis has been divided by $\Delta\nu$, and the stacked spectra have been sorted by $\nu_{\max}/\Delta\nu$. Panels (a) and (c) highlight lower radial-order ridges, while Panels (b) and (d) show higher ν_{\max} values in a wider range. Red lines in the bottom panels indicate $l = 1, 2, 0$ pulsation ridges predicted by model frequencies, which shows an excellent match with the data. Integers on the top of each panel mark radial orders given by model frequencies, which are confirmed by peak-bagging (see Section 6.2). The green dashed lines connect for each star a radial mode that is closest to ν_{\max} (also shown in Figure 2b).

involved 20 (0.8%) stars, and the clear ridges for these stars shown in Figures 7a and 8a ensure its reliability to reveal the regular frequency patterns.

(iii) For each target spectrum, we searched for its best-matching template spectrum by choosing the one whose maximum cross-correlation with the target spectrum is the largest. We then shifted the target spectrum with respect to the best-matching template spectrum by an offset equal to the lag of the maximum cross-correlation. When the shifted spectra were stacked they form clear ridges, as seen in Figure 7 and 8. Note that a spectrum was not used if the shift was greater than $1/2 \Delta\nu$, to avoid the observed and template spectra being mismatched by one or more radial orders (only 7 stars were discarded in this step). From the best-matching template spectrum, its theoretical frequencies were used to determine the radial order and angular degree for the dominant mode, which were used in Section 3.

(iv) Lastly, we sorted the shifted observed spectra by ν_{\max} for Figure 7 and by $\nu_{\max}/\Delta\nu$ for Figure 8. Here, the values

of ν_{\max} and $\Delta\nu$ the ones corresponding to the best-matching template spectra.

Figure 7 displays the radial orders of $l = 0$ modes measured from the model frequencies as indicated at the top of each panel (the values of n hereafter refer to the radial order of $l = 0$ modes, unless specifically stated). We have used an independent method to confirm this radial order assignment, which will be presented in the next section. [Stello et al. \(2014\)](#) firstly recognized triplet structures that consist of dipole ($l = 1$) modes to the left, quadrupole ($l = 2$) modes in the middle, and radial ($l = 0$) modes to the right. The so-called f -mode ridge ([Stello et al. 2014](#)), which would lie to the left of the ridge $[n, l] = [1, 0]$, is not clearly detected. In Figure 7 we can see the triplet structure is gradually resolved towards larger ν_{\max} values and higher radial orders.

We again show the stacked power spectrum in Figure 8, now with the horizontal axes divided by $\Delta\nu$. Figure 8 shows sub-ridges related to multiple angular degrees. Here, we can

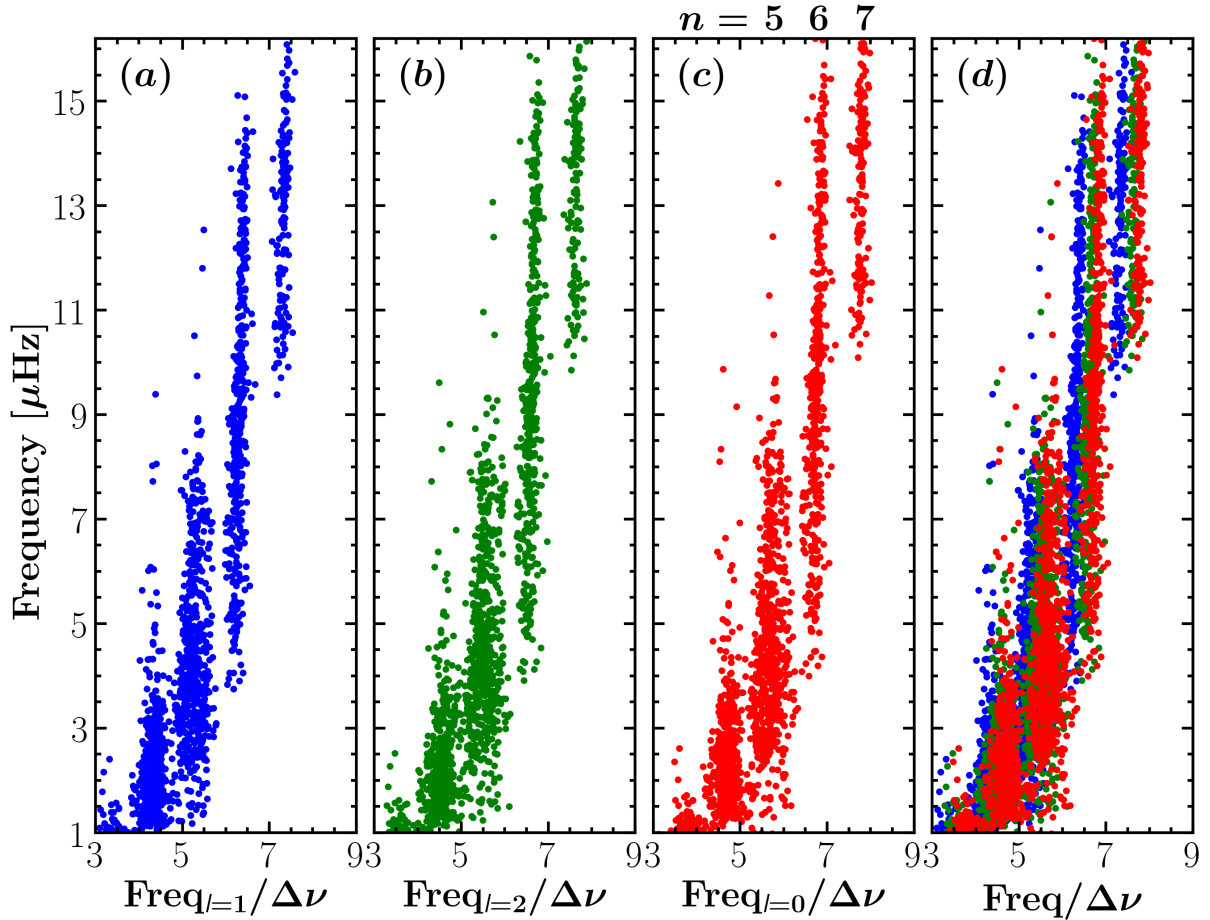


Figure 9. Oscillation patterns for (a) $l = 1$, (b) $l = 2$, and (c) $l = 0$ modes of high-luminosity red giants. (d) The combination of the $l = 1, 2, 0$ oscillation patterns. The horizontal axes are the frequency divided by measured $\Delta\nu$, while the vertical axes are frequency. For each star only one $l = 1, 2$, and 0 mode are shown.

see the ridge of the first radial overtone ($n = 2$) is marginally resolved in the range $0.45 \mu\text{Hz} \leq \nu_{\text{max}} \leq 0.64 \mu\text{Hz}$, and the individual components of the triplet structure gradually merge towards the lower- ν_{max} end. Longer light curves are thus required to resolve triplet structures for the radial order $n = 2$ and $\nu_{\text{max}} < 0.45 \mu\text{Hz}$, and for the entire ridge of the radial fundamental mode. The red lines in the lower panels of Figure 8 indicate the model frequencies, which match the observations well.

The well-resolved ridges separated by the so-called small and large frequency separations for various radial orders at such late evolutionary phase (ν_{max} down to $0.14 \mu\text{Hz}$) resemble the ridges seen in less-luminous red giants (e.g. Mosser et al. 2011). This implies that the asymptotic relation of acoustic modes remains helpful for assigning radial orders and angular degrees, although the relation is expected to break down at low radial orders. The asymptotic relation is given as (Tassoul 1980):

$$\nu_{n,l} = \Delta\nu\left(n + \frac{l}{2} + \epsilon\right) - \delta\nu_{0,l}, \quad (2)$$

where $\nu_{n,l}$ is the eigenfrequency at radial order n and angular degree l , ϵ is an offset parameter, and $\delta\nu_{0,l}$ is the small frequency separation between radial and non-radial modes.

6.2 Radial order assignment by peak-bagging

In order to confirm the radial order assignment given by model frequencies, we aim to determine the radial orders from the observations by measuring mode frequencies, $\Delta\nu$ and ϵ . For this, one of the most important steps is to make good initial guesses of mode frequencies. Here, for each star we used the frequencies from the best-matching template spectrum, as defined in Section 6.1. We then fitted three Lorentzian profiles to the $l = 1, 2, 0$ modes. Only the triplet structure with the largest power was picked.

Figure 9 shows oscillation patterns of $l = 1, 2, 0$ modes for stars with $\nu_{\text{max}} > 1.0 \mu\text{Hz}$. This is analogous to the pattern seen in higher- ν_{max} red giants (Bedding et al. 2010; Huber et al. 2010; Mosser et al. 2011), here restricted to low- ν_{max} stars. The horizontal scatter increases with decreasing radial order, which is mainly because the mean large frequency separation $\Delta\nu$ is less well defined towards lower- ν_{max} stars. For these low- ν_{max} stars, only a few orders of modes are excited, and modes with the same angular degrees deviate significantly from equally spaced).

To assign a radial order using Equation 2, we started with the two ridges on the far right in Figure 9c ($n = 6, 7$). This is because (1) for radial modes, the small frequency

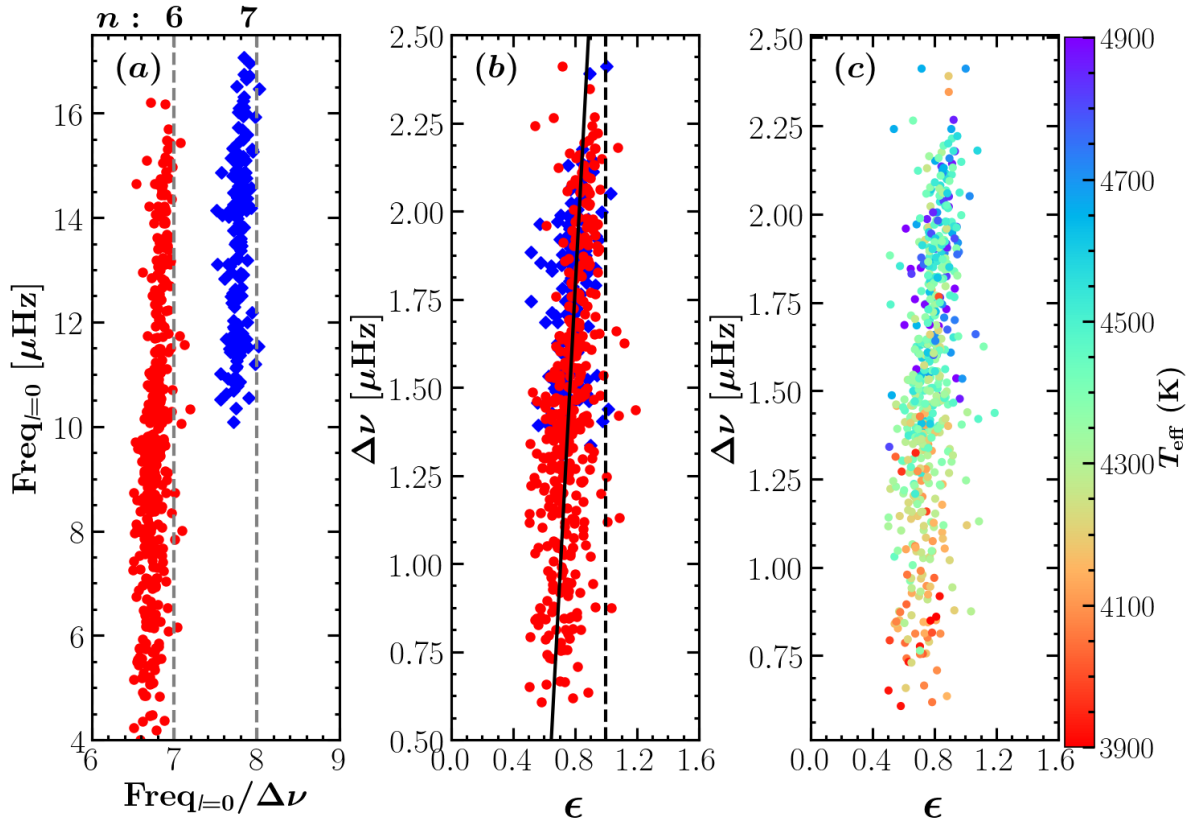


Figure 10. (a) Same as Figure 9c now only for the two ridges for which we aim to measure their radial orders. (b) The relation between $\Delta\nu$ and ϵ , where ϵ is measured via Equation 2 by assigning a radial order of 6 to the ridge in red and 7 to the ridge in blue. (c) Same as (b) now color-coded by effective temperature.

separation term, $\delta\nu_{0,l}$, is zero; (2) the associated $\Delta\nu$ can be measured more precisely, as indicated by the much smaller scatter, compared to the $n = 4$ and 5 ridges; (3) the asymptotic relation works more accurately at higher radial orders; and (4) the lower radial order can be easily deduced once higher radial orders are identified.

Figure 10a shows the two radial-mode ridges with ν_{\max} in the range $4 \mu\text{Hz} < \nu_{\max} < 17 \mu\text{Hz}$. Figure 10b shows $\Delta\nu$ as a function of the offset ϵ that was computed by using Equation 2 and by assuming $n = 6$ for the red ridge and $n = 7$ for the blue ridge. Clearly, the ϵ values are collectively smaller than unity, which is in agreement with Mosser et al. (2011) and Kallinger et al. (2012) for the stars in their samples that overlap in ν_{\max} with ours. This result confirms the ridges in red and blue correspond to the radial orders of 6 and 7, respectively. This radial order assignment is thus consistent with the assignment given by the model frequencies as shown above. Figure 10c shows that for our sample the offset ϵ is an increasing function of $\Delta\nu$, and $\Delta\nu$ is an increasing function of effective temperature (see the colourbar). This means ϵ increases with increasing effective temperature. This relation between the offset ϵ and effective temperature has also been found in both dwarfs and giants (White et al. 2011, 2012; Lund et al. 2017). With $n = 6$ and $n = 7$ confirmed, the identifications for $n = 1$ to 5 follows from the discussions in Section 6.1.

To summarize, from the analyses in Section 6 and the

comparison between the *Kepler* and OGLE LPVs (Figure 4b), we provide a solution to the open question on the radial order assignment of LPVs as detailed in the introduction. Our results confirm that the radial orders of $n=1, 2, 3$, and 4 can be used to explain the sequences C, C' and B combined, A, and A' in the P–L diagram, respectively, which is consistent with the recent theoretical explanations by Trabucchi et al. (2017).

7 ARE DIPOLE MODES DOMINANT AMONG THE PULSATIONS OF LPVs?

Which modes are dominant, radial or non-radial modes? To answer this question, we measured relative amplitudes of $l = 0, 1, 2$ modes for the radial orders $1 \leq n \leq 6$.

In order to measure the amplitude for a given n and l , we used the stacked power spectrum, as shown in Figure 8, and summed up the amplitude along the associated ridge indicated by the red lines in Figures 8c and 8d. The collapsed total amplitude was evaluated over the ν_{\max} ranges equal to the length of the red lines. For each star, its background-divided power spectrum was normalized so that the amplitude of the highest peak was unity. Lastly, for each radial order, the collapsed amplitude was normalized to set its highest peak to unity. The results are shown in Figure 11.

Figure 11a shows only a single peak for $n = 1$. Inter-

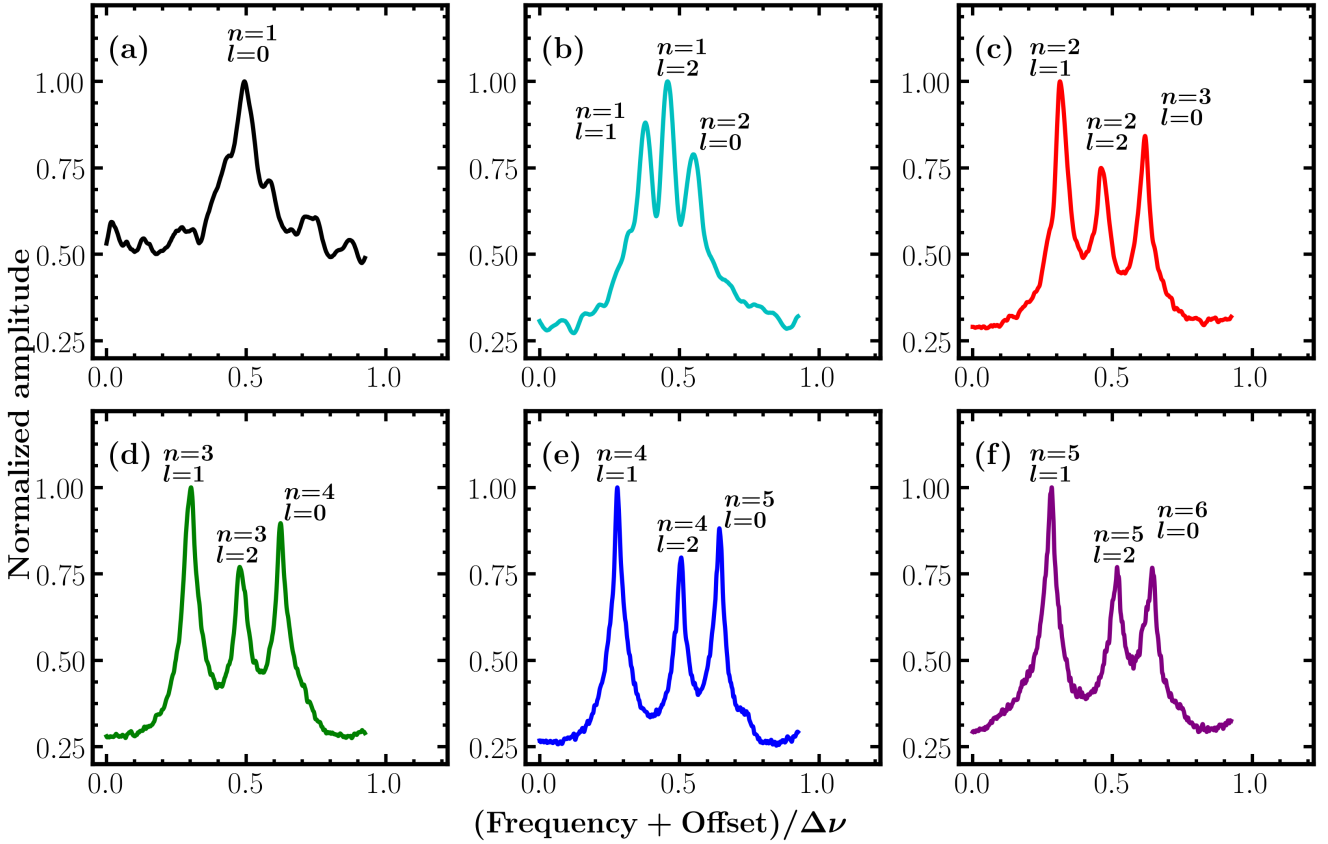


Figure 11. Relative amplitude of $l = 1, 2, 0$ modes across various radial orders, as indicated by the legends. As an example, the three peaks from left to right in Panel (b) correspond to $(n, l) = (1, 1)$, $(1, 2)$, and $(2, 0)$ modes, respectively. Dipole modes are dominant in the radial orders of $n = 3, 4, 5, 6$, while quadrupole modes are dominant in the radial order of $n = 2$. The triplet structure shrinks gradually toward lower radial orders, and merges eventually in the radial orders of $n = 1$.

estingly, for $n = 2$ (note radial orders are defined for $l = 0$ modes in this work), the middle peak ($l = 2$ modes) is globally the highest. This property is distinct from the higher radial orders $3 \leq n \leq 6$, for which all the collectively dominant modes are dipole modes. Note that, as shown in Figure 8c, for radial order $n = 2$ the dominant $l = 2$ mode is marginally visible at $\nu_{\max} \approx 0.55 \mu\text{Hz}$, and the $l = 2, 0$ ridges are gradually merged as ν_{\max} decreases.

Our result yields an average $l = 1$ visibility $V_1^2 = 1.5$ (averaged over $n=2, 3, 4, 5$, and 6) and an average $l = 2$ visibility $V_2^2 = 0.7$ (averaged over $n = 3, 4, 5$, and 6), and thus are consistent with the theoretical prediction ($V_1^2 = 1.5$, $V_2^2 = 0.6$) and with the observed values ($V_1^2 = 1.3$, $V_2^2 = 0.6$) for the solar-like oscillations in red giants (see Mosser et al. 2012, and references therein).

Our findings of the dominant $l = 1$ modes with radial order $n \geq 3$ are consistent with the results by Mosser et al. (2013) (see their Figure 9) and Stello et al. (2014). However, the findings of the dominant $l = 2$ modes in radial order $n = 2$ (at least in a higher ν_{\max} range) is discrepant to Mosser et al. (2013) who argued that radial modes are dominant when $\nu_{\max} \lesssim 1.0 \mu\text{Hz}$. We note Stello et al. (2014) clearly detected the $n = 2$ ridge but did not resolve the associated sub-ridges.

Another interesting feature shown in Figure 11 is that the triplet structure gets more narrow with decreasing ra-

dial order. This feature makes it difficult to resolve multiple angular degrees, given the 4-year baseline of *Kepler* light curves. The closely spaced triplet structures are very different in the LPVs than in less-luminous red giants. For the latter, $l = 1$ modes are nearly located at the midpoint of adjacent $l = 0$ modes (e.g. Huber et al. 2010, see their Figure 10). OGLE data will be valuable for studying the unresolved or marginally resolved triplet structures, thanks to 4 years of data set from the OGLE-II project and 8 years of observations from the OGLE-III project. This will be presented in a future paper.

8 TESTING SEISMIC SCALING RELATIONS FOR HIGH-LUMINOSITY RED GIANTS

Since the seismic scaling relations provide an efficient way to derive stellar fundamental properties, such as mass and radius, their validity has been extensively tested on dwarfs and giants (see Chaplin & Miglio 2013; Hekker & Christensen-Dalsgaard 2017, for reviews). It seems inevitable that the seismic scaling relations should break down at a certain evolutionary stage, at least in Mira variables in which pulsations are self-excited via a heat-engine mechanism, which is different from solar-like oscillations. We will test the seismic scaling relations for high-luminosity red giants.

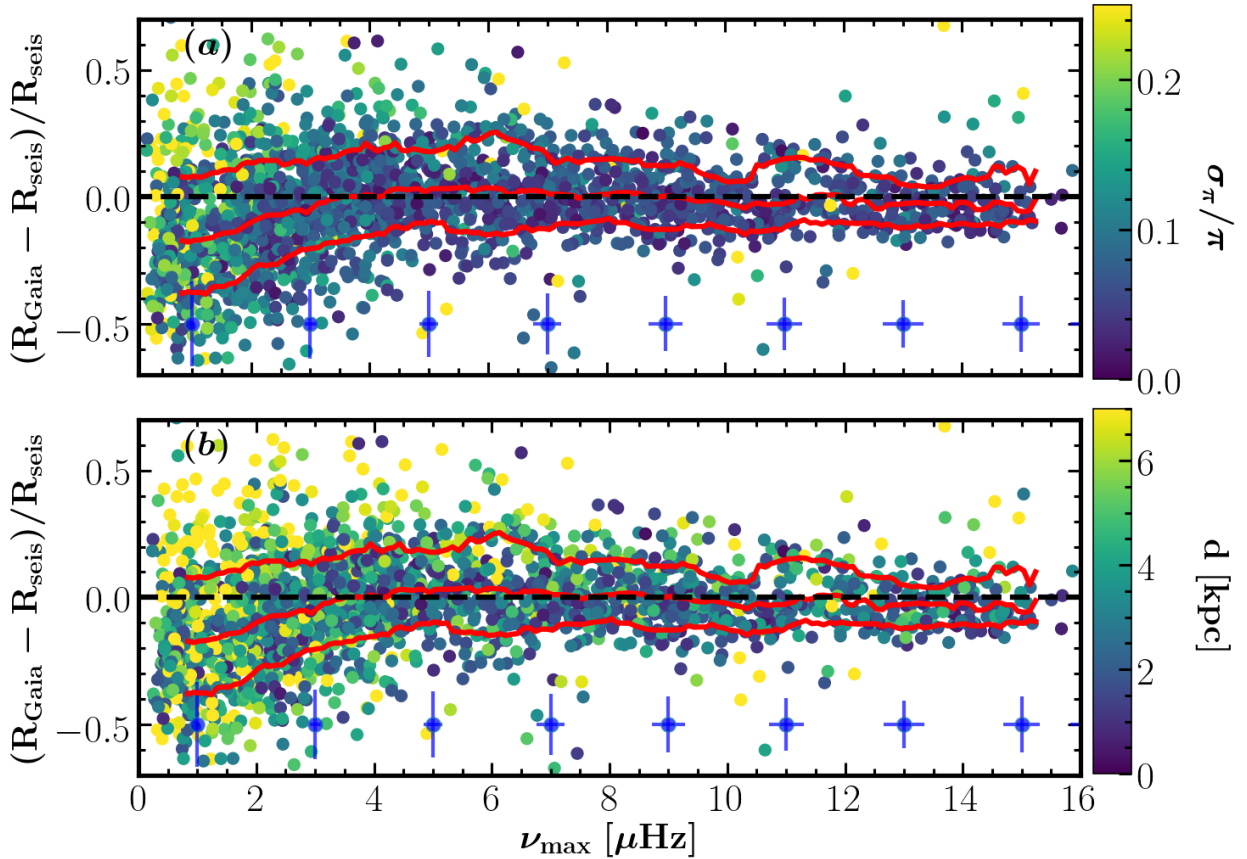


Figure 12. (a) Relative radius difference as a function of ν_{\max} , color-coded by (a) the fractional uncertainty of Gaia DR2 parallax and (b) distance derived using the method by Huber et al. (2017) and Berger et al. (2018). The 16th, 50th, and 84th percentiles are indicated by the red lines in each panel. The median uncertainty in each ν_{\max} bin in steps of $2 \mu\text{Hz}$ are indicated.

Figure 12 shows a comparison between radii calculated from the seismic scaling relations and radii derived from the Gaia DR2 parallaxes (Lindegren et al. 2018). To calculate the seismic radii, we use the following relation:

$$\frac{R}{R_{\odot}} \simeq \left(\frac{\nu_{\max}}{\nu_{\max\odot}} \right) \left(\frac{\Delta\nu}{\Delta\nu_{\odot}} \right)^{-2} \left(\frac{T_{\text{eff}}}{T_{\text{eff}\odot}} \right)^{1/2}, \quad (3)$$

where the solar references are $\nu_{\max\odot} = 3090 \mu\text{Hz}$, $\Delta\nu_{\odot} = 135.1 \mu\text{Hz}$ (Huber et al. 2011), and $T_{\text{eff}\odot} = 5777 \text{ K}$. The global seismic parameters, ν_{\max} and $\Delta\nu$, were measured using the SYD pipeline (Huber et al. 2009), which gave very good agreement with Yu et al. (2018) (The mean differences were 0.8% in ν_{\max} and 0.2% in $\Delta\nu$ for 692 stars in common) and Pinsonneault et al. (2018) (The mean differences were 1.3% in ν_{\max} and 0.2% in $\Delta\nu$ for 531 stars in common). Effective temperatures in this work were adopted from Mathur et al. (2017), which were mainly based on photometry, and are also consistent with APOGEE spectroscopic temperatures from Pinsonneault et al. (2018). We then derived radii from Gaia DR2 parallaxes using the same method as Huber et al. (2017) and Berger et al. (2018). We applied a cut to fractional parallax uncertainty, namely, $\sigma_{\pi}/\pi < 0.6$. From this, we obtained a sample of 2241 LPVs with both seismic and parallax-based radii available.

Figure 12 shows the relative radius difference as a func-

tion of ν_{\max} , colour-coded by the fractional uncertainty of Gaia DR2 parallax, σ_{π}/π , and distance. We can see that the radii derived from the two independent methods are consistent when $\nu_{\max} \gtrsim 3 \mu\text{Hz}$. This suggests that the seismic scaling relations remain accurate for luminous red giants ($\nu_{\max} \gtrsim 3 \mu\text{Hz}$, $R \lesssim 40 R_{\odot}$, or $\log L/L_{\odot} \lesssim 2.6$). Lindegren et al. (2018) suggested Gaia DR2 parallaxes are too small by 0.03 mas, thus we added this systematic offset to the parallaxes for individual stars when computing their parallax-based radii. This remarkable consistency confirms the existence of the 0.03 mas zero-point offset in Gaia DR2 parallaxes. We also tested the parallax zero-point correction method proposed by Zinn et al. (2019), where the median correction value was 0.065 mas for our sample. The results shows that the parallax-based radii were 7% smaller than the seismically derived radii. The discrepancy in the different parallax zero-point corrections might be linked to the different star samples where our stars are more luminous than those used by Zinn et al. (2019) for their calibration.

Figure 12 also shows that the relative radius difference increases with decreasing ν_{\max} when $\nu_{\max} \lesssim 3 \mu\text{Hz}$. This increasing systematic offset suggests that the seismic scaling relations is likely to gradually break down at $\nu_{\max} \lesssim 3 \mu\text{Hz}$. This ν_{\max} threshold tells us that the seismic scaling relations

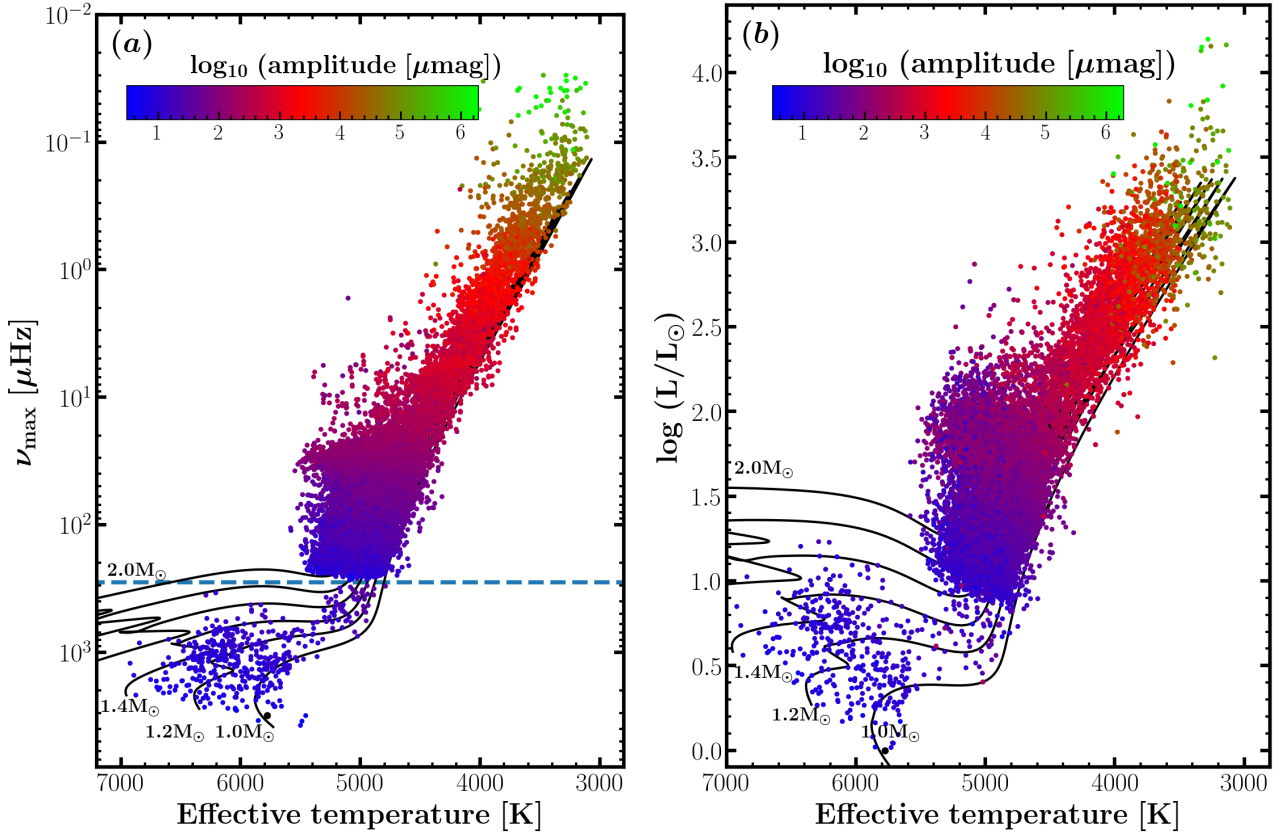


Figure 13. (a) Seismic H-R diagram (ν_{\max} vs T_{eff}). The estimates of ν_{\max} and oscillation amplitude were adopted from Huber et al. (2011) for main-sequence and subgiant stars, Yu et al. (2018) for low/intermediate luminosity red giants, and this work for high-luminosity red giants ($\nu_{\max} < 15 \mu\text{Hz}$). The color bar indicates the oscillation amplitude of the radial mode for the stars from the literature, and the amplitude proxy for the stars analysed in this work. We take effective temperatures from Mathur et al. (2017), and update them wherever temperature is cooler than 3200 K (for the scheme see the text). The dashed line indicates the long-cadence Nyquist frequency, below which it is very challenging to detect the oscillations using the *Kepler* long cadence data. (b) H-R diagram. The values of luminosity are calculated from Gaia DR2 parallaxes, either from this work or Berger et al. (2018).

may not be applicable to SRs, which typically have a $\nu_{\max} < 0.5 \mu\text{Hz}$.

From Figure 12, we can see that the dispersion is mainly caused by the uncertainties. We carried out two-sided one sample t-tests to confirm the validity of the seismic scaling relations in the regimes $\nu_{\max} > 3 \mu\text{Hz}$ and $\nu_{\max} \leq 3 \mu\text{Hz}$.

In both cases, our null hypothesis was that the seismic and Gaia-based radii are not significantly different. In other words, we hypothesized $(R_{\text{Gaia}} - R_{\text{seis}})/R_{\text{seis}} = 0$. For the $\nu_{\max} > 3 \mu\text{Hz}$, we found that the t-statistic value is -0.18, which we used to calculate a p-value along with the degrees of freedom $n - 1 = 1342$. The p-value is 0.85, which is far greater than the significance level $\alpha = 0.05$, so we accepted our null hypothesis. This means there is no statistically significant difference between the seismic and Gaia-based radii.

For $\nu_{\max} \leq 3 \mu\text{Hz}$, we found that the t-statistic value is -13.94. Together with the degrees of freedom $n - 1 = 888$, we obtained a p-value of 4.01×10^{-40} . The p-value is far less than the significance level $\alpha = 0.05$, so we rejected the null hypothesis. This means the seismic radii are statistically significantly different from the Gaia-based radii.

9 HERTZSPRUNG-RUSSELL DIAGRAM OF *Kepler* OSCILLATORS

Figure 13a shows a seismic H-R diagram, color-coded by the oscillation amplitude per radial mode. We note that for the stars in our sample with $T_{\text{eff}} < 3200\text{K}$ from Mathur et al. (2017), T_{eff} was poorly determined. For this, we updated their temperatures by using $g-K_s$ colour calculated from SDSS g and 2MASS K_s magnitude and following the empirically calibrated scheme from Huang et al. (2015). Extinctions were calculated using the method by Huber et al. (2017) and Berger et al. (2018) and corrected by adopting the extinction laws from Yuan et al. (2013). Since ν_{\max} and amplitude cannot be measured for all the stars in our high-luminosity red-giant sample in the same way as for lower-luminosity stars, we used the frequency and height of the highest peak to represent ν_{\max} and the oscillation amplitude. We note that the group of Miras (green dots) have higher amplitudes than expected from the trend of the stars with higher ν_{\max} . This is because pulsations in Miras are driven differently from the rest of the sample. This seismic H-R diagram indicates that both ν_{\max} and the amplitude span more than six orders of magnitude, which represents so far the largest parameter ranges measured only from observations.

Considering the availability of Gaia DR2 parallaxes for almost all of the stars shown in Figure 13a, we plot a H-R diagram as shown in Figure 13b, where luminosities were computed from Gaia DR2 parallaxes either from this work for our sample or from Berger et al. (2018) for the rest of the stars shown in Figure 13b. We can see the red clump with a relatively large scatter.

It is challenging to distinguish RGB from AGB stars with similar effective temperatures and luminosities, although Mosser et al. (2014) have found a few dozens of stars leaving the main region of the red clump on their way to ascend the AGB. The tip of the RGB (TRGB) is a key feature in the H-R diagram where the density of star number starts to decrease significantly, allowing one to clearly identify stars in the AGB phase as those beyond the TRGB. This feature is, however, not clearly seen in Figure 13b, which is caused by the limited sample size of stars near the TRGB and the large luminosity uncertainties. Although the ν_{\max} estimates are more precise, the TRGB is still not clearly seen in Figure 13a.

10 CONCLUSIONS

We carried out asteroseismic analyses of high-luminosity *Kepler* red giants with pulsation periods $P \gtrsim 1$ day. We attempted to address open questions regarding the excitation mechanisms, radial order assignment, and dominant mode nature (radial or non-radial). We also investigated the relation between pulsation amplitude and period for low- ν_{\max} sun-like oscillators ($\nu_{\max} \lesssim 10\mu\text{Hz}$), SRs, and Mira variables. For the first time we performed a test on the validity of the seismic scaling relations with high-luminosity *Kepler* red giants using Gaia DR2 parallaxes. The main results are summarized below:

(i) By comparing the amplitudes measured from full-length *Kepler* and OGLE light curves and 1/3 shorter segments of the light curves, SRs are confirmed to be stochastically excited as solar-like oscillators, which is different from self-excited Mira variables. Using the same method, we find Mira variables have much longer mode lifetime than SRs, and the lifetime of SRs changes continuously (see Figure 5).

(ii) We have made an unambiguous detection of well-resolved pulsation ridges, corresponding to radial fundamental mode and overtones ($2 \leq n \leq 7$), and sub-ridges, linked to $l = 0, 1, 2$ modes (see Figure 7). Our radial order assignment from the two ways (model frequencies and peak-bagging) is consistent with Stello et al. (2014), and Mosser et al. (2013) for $n \geq 3$ but not for $n = 2$ (see Figure 8 and 9).

(iii) Clear pulsation sequences on the P-L diagram have not been detected in *Kepler* LPVs, which are expected to be present as for the OGLE LPVs in the LMC. The approximate six times larger uncertainty in absolute magnitude, σ_{M_K} , for *Kepler* LPVs makes the ridges difficult to be detected (see Figure 4).

(iv) We show that the $l = 1$ modes are dominant in the overtones of $n=3, 4, 5$, and 6, while the $l = 2$ modes appear to be dominant in the first overtone $n = 2$ (see Figure 11). Since the triplet structure gets gradually closer with decreasing pulsation frequency, longer time series are required to resolve multiple angular degrees. OGLE light curves with a typical baseline of 8 years, with an extension to 12 years for some

pulsators, are thus very valuable to resolve the first overtone and radial fundamental modes.

(v) A comparison of radii computed from the scaling relations to those derived from Gaia DR2 parallaxes shows good agreement, with an increasing systematic offset when $\nu_{\max} \lesssim 3\mu\text{Hz}$ ($R \gtrsim 40 R_{\odot}$, or $\log L/L_{\odot} \gtrsim 2.6$). This suggests the seismic scaling relations could break down in this regime. On the other hand, the comparison shows an excellent agreement where $\nu_{\max} \gtrsim 3\mu\text{Hz}$, implying that the scaling relations are still accurate. This also confirms the existence of the 0.03 mas systematic offset in Gaia DR2 parallaxes (see Figure 12).

TESS will observe bright stars in nearly the whole sky and provide up to one year of time series for targets in the continuous viewing zones. These upcoming new data will permit the detection of known and potentially new LPVs, in particularly these with periods around 60 days, which has been argued as a threshold of substantial pulsation-triggered mass loss (McDonald & Zijlstra 2016). The supplementary ground-based spectroscopic observations and the high-quality parallaxes from Gaia and *Hipparcos* enable us to investigate the relation between luminosity, metallicity, and pulsation, and hence shed light on the mechanism transition in mass loss from magneto-acoustic wind to pulsation wind (McDonald et al. 2018).

ACKNOWLEDGEMENTS

We are thankful for the referee's careful reading of the manuscript and helpful comments and suggestions. We thank Jennifer van Saders, James S. Kuszewicz, Nathalie Themessl, and Patrick Gaulme for their useful comments and discussions. We gratefully acknowledge the entire *Kepler* team and everyone involved in the *Kepler* mission for making this paper possible. Funding for the *Kepler* Mission is provided by NASA's Science Mission Directorate. This work was supported in part by the German space agency (Deutsches Zentrum für Luft- und Raumfahrt) under PLATO data grant 500O1501. The computational resources were provided by the German Data Center for SDO through a grant from the German Aerospace Center (DLR). This work is partially supported by the Joint Research Fund in Astronomy (U1631236) under cooperative agreement between the National Natural Science Foundation of China (NSFC) and Chinese Academy of Sciences (CAS). D.H. acknowledges support by the National Science Foundation (AST-1717000). D.S. is the recipient of an Australian Research Council Future Fellowship (project number FT1400147). The research leading to the presented results has received funding from the European Research Council under the European Community's Seventh Framework Programme (FP7/2007-2013) / ERC grant agreement no 338251 (StellarAges).

REFERENCES

- Bányai E., et al., 2013, *MNRAS*, **436**, 1576
- Bedding T. R., 2003, *Ap&SS*, **284**, 61
- Bedding T. R., Zijlstra A. A., 1998, *ApJ*, **506**, L47
- Bedding T. R., et al., 2010, *ApJ*, **713**, L176

- Berger T. A., Huber D., Gaidos E., van Saders J. L., 2018, *ApJ*, **866**, 99
- Borucki W. J., et al., 2010, *Science*, **327**, 977
- Chaplin W. J., Miglio A., 2013, *ARA&A*, **51**, 353
- Chaplin W. J., et al., 2011, *Science*, **332**, 213
- Chaplin W. J., et al., 2013, *ApJ*, **766**, 101
- Christensen-Dalsgaard J., 2008, *Ap&SS*, **316**, 113
- Christensen-Dalsgaard J., Kjeldsen H., Mattei J. A., 2001, *ApJ*, **562**, L141
- Dziembowski W. A., Soszyński I., 2010, *A&A*, **524**, A88
- Feast M. W., 1996, *MNRAS*, **278**, 11
- Ferreira Lopes C. E., et al., 2015, *A&A*, **583**, A122
- Foreman-Mackey D., Agol E., Ambikasaran S., Angus R., 2017, *AJ*, **154**, 220
- Hartig E., Cash J., Hinkle K. H., Lebzelter T., Mighell K. J., Walter D. K., 2014, *AJ*, **148**, 123
- Hekker S., 2019, arXiv e-prints, p. arXiv:1907.10457
- Hekker S., Christensen-Dalsgaard J., 2017, *A&ARv*, **25**, 1
- Huang Y., Liu X.-W., Yuan H.-B., Xiang M.-S., Chen B.-Q., Zhang H.-W., 2015, *MNRAS*, **454**, 2863
- Huber D., Stello D., Bedding T. R., Chaplin W. J., Arentoft T., Quirion P.-O., Kjeldsen H., 2009, *Communications in Asteroseismology*, **160**, 74
- Huber D., et al., 2010, *ApJ*, **723**, 1607
- Huber D., et al., 2011, *ApJ*, **743**, 143
- Huber D., et al., 2017, *ApJ*, **844**, 102
- Imara N., Blitz L., 2007, *ApJ*, **662**, 969
- Kallinger T., et al., 2012, *A&A*, **541**, A51
- Koch D. G., et al., 2010, *ApJ*, **713**, L79
- Lebzelter T., 2011, *A&A*, **530**, A35
- Lebzelter T., Schultheis M., Melchior A. L., 2002, *A&A*, **393**, 573
- Lebzelter T., Mowlavi N., Marigo P., Pastorelli G., Trabucchi M., Wood P. R., Lecoœur-Taïbi I., 2018, *A&A*, **616**, L13
- Lindgren L., et al., 2018, *A&A*, **616**, A2
- Lund M. N., 2019, *MNRAS*, **489**, 1072
- Lund M. N., et al., 2017, *ApJ*, **835**, 172
- Mathur S., et al., 2017, *ApJS*, **229**, 30
- Mathur S., García R. A., Bugnet L., Santos Â. R. G., Santiago N., Beck P. G., 2019, *Frontiers in Astronomy and Space Sciences*, **6**, 46
- McDonald I., Zijlstra A. A., 2016, *ApJ*, **823**, L38
- McDonald I., De Beck E., Zijlstra A. A., Lagadec E., 2018, *MNRAS*, **481**, 4984
- Mosser B., et al., 2011, *A&A*, **525**, L9
- Mosser B., et al., 2012, *A&A*, **537**, A30
- Mosser B., et al., 2013, *A&A*, **559**, A137
- Mosser B., et al., 2014, *A&A*, **572**, L5
- Mowlavi N., et al., 2018, *A&A*, **618**, A58
- Paxton B., Bildsten L., Dotter A., Herwig F., Lesaffre P., Timmes F., 2011, *ApJS*, **192**, 3
- Paxton B., et al., 2013, *ApJS*, **208**, 4
- Pinsonneault M. H., et al., 2018, *ApJS*, **239**, 32
- Rasmussen C., Williams C., 2006, *Gaussian Processes for Machine Learning. Adaptive Computation and Machine Learning*, MIT Press, Cambridge, MA, USA
- Ricker G. R., et al., 2015, *Journal of Astronomical Telescopes, Instruments, and Systems*, **1**, 014003
- Schonhut-Stasik J., et al., 2019, arXiv e-prints, p. arXiv:1910.03803
- Smith J. C., et al., 2012, *PASP*, **124**, 1000
- Soszyński I., Wood P. R., 2013, *ApJ*, **763**, 103
- Soszyński I., Udalski A., Kubiak M., Szymanski M., Pietrzynski G., Zebun K., Szewczyk O., Wyrzykowski L., 2004, *Acta Astron.*, **54**, 129
- Soszyński I., et al., 2007, *Acta Astron.*, **57**, 201
- Soszyński I., et al., 2009, *Acta Astron.*, **59**, 239
- Stello D., et al., 2014, *ApJ*, **788**, L10
- Stumpe M. C., et al., 2012, *PASP*, **124**, 985
- Tabur V., Bedding T. R., Kiss L. L., Giles T., Derekas A., Moon T. T., 2010, *MNRAS*, **409**, 777
- Takayama M., Saio H., Ita Y., 2013, *MNRAS*, **431**, 3189
- Tassoul M., 1980, *ApJS*, **43**, 469
- Trabucchi M., Wood P. R., Montalbán J., Marigo P., Pastorelli G., Girardi L., 2017, *ApJ*, **847**, 139
- White T. R., Bedding T. R., Stello D., Christensen-Dalsgaard J., Huber D., Kjeldsen H., 2011, *ApJ*, **743**, 161
- White T. R., et al., 2012, *ApJ*, **751**, L36
- Wood P. R., 2015, *MNRAS*, **448**, 3829
- Wood P. R., et al., 1999, in Le Bertre T., Lebre A., Waelkens C., eds, *IAU Symposium Vol. 191, Asymptotic Giant Branch Stars*. p. 151
- Xiong D. R., Deng L., Zhang C., 2018, *MNRAS*, **480**, 2698
- Yu J., Huber D., Bedding T. R., Stello D., Hon M., Murphy S. J., Khanna S., 2018, *ApJS*, **236**, 42
- Yuan H. B., Liu X. W., Xiang M. S., 2013, *MNRAS*, **430**, 2188
- Zinn J. C., Pinsonneault M. H., Huber D., Stello D., 2019, *ApJ*, **878**, 136

This paper has been typeset from a $\text{\TeX}/\text{\LaTeX}$ file prepared by the author.